Science

REPORTS

Cite as: Z. Tao *et al.*, *Science* 10.1126/science.aaf6793 (2016).

Direct time-domain observation of attosecond final-state lifetimes in photoemission from solids

Zhensheng Tao,[1]*† Cong Chen,[1]*† Tibor Szilvási,[2] Mark Keller,[3] Manos Mavrikakis,[2] Henry Kapteyn,[1] Margaret Murnane[1]

[1]Department of Physics and JILA, University of Colorado and NIST, Boulder, CO 80309, USA. [2]Department of Chemical and Biological Engineering, University of Wisconsin, Madison, WI 53706, USA. [3]National Institute of Standards and Technology (NIST), Boulder, CO 80305, USA.

* Corresponding author. Email: zhensheng.tao@jila.colorado.edu (Z.T.); cong.chen@colorado.edu (C.C.)

†These authors contributed equally to this work.

Recently, attosecond spectroscopic techniques have made it possible to measure differences in transport times for photoelectrons from localized core levels and delocalized valence bands in solids. Here, we report the application of attosecond pulse trains to directly and unambiguously measure the difference in lifetimes between photoelectrons born into free-electron-like states and those excited into unoccupied excited states in the band structure of nickel (111). A significant increase in lifetime of 212 ± 30 as occurs when the final state coincides with a short-lived excited state. Moreover, a strong dependence of this lifetime on emission angle is directly related to the final-state band dispersion as a function of electron transverse momentum. This finding emphasizes the importance of the material band structure on photoemission lifetimes and corresponding electron escape depths.

The electronic band structure of materials consists of occupied and unoccupied bands that emerge as the electron wavefunctions of adjacent atoms in the lattice overlap with each other. In general, valence bands will have more wavefunction overlap, and will therefore be wider than, for example, the core levels. The periodicity of a crystal lattice imposes an energy-momentum relation that is described as the dispersion relationship for electrons in each band, making the electronic structure of solids quite complex. Fortunately, angle-resolved photoemission spectroscopy (ARPES) can resolve both the energy and momentum of photoelectrons by probing photoemission from materials at well-defined angles. This information is directly related to the energy and momentum of electrons populating distinct bands, providing detailed information about band dispersion and the Fermi surface (*1*). When combined with ultrafast lasers, time-resolved ARPES makes it possible to capture fast changes in the band structure of materials near the center of the Brillouin zone (i.e. low electron momenta) on picosecond (ps) and femtosecond (fs) time scales (*2*). More recently, advances in tabletop high-harmonic generation (HHG) (*3*, *4*) have resulted in coherent extreme ultraviolet (EUV) and soft X-ray beams that are ideally suited for ARPES, opening up time-resolved studies over the entire Brillouin zone (*5*, *6*). HHG is emitted as a series of attosecond pulse trains with unique characteristics of good energy resolution (≈100-300 meV), combined with sub-fs time resolution. These capabilities have made it possible to observe and control the fastest electron dynamics in molecular and material systems (*7*, *8*). Recent work probed how fast a material can change its magnetic state or transition from insulating to metallic (*5*, *9*), uncovering which microscopic mechanisms were responsible for driving fast phase or state transitions in materials. Other work probed the ≈ 7 fs lifetime of core-excited states of adsorbates on surfaces (*10*).

The time delay associated with the photoemission process itself has been probed in isolated atoms and materials using HHG (*11*–*17*), by taking advantage of laser-assisted photoemission (*18*). Although some discrepancy remains between experiment and theory (*17*, *19*), it is generally agreed that the photoemission time delay from isolated atoms arises from convolution of a Wigner time delay due to scattering of photoelectrons in the atomic potential and a measurement-induced delay due to propagation of the photoelectrons in the laser field (*20*). Compared to the case of isolated atoms, interpreting photoemission time delays from solids requires consideration of complex band structures and various many-body interactions that photoelectrons can experience as they approach the surface. Previous attosecond-streaking studies of a transition-metal W (110) surface revealed a considerable time delay (~110 as) between photoemission from core-level and valence-band states (*11*). In contrast, no delay was measured for the free-electron metal Mg, although a similar time delay to W was expected

(*13*). Various theoretical models have been proposed to explain the photoemission time delay from solids in terms of transport time (*21*, *22*), degrees of initial-state localization (*21*, *23*), and band-structure effects (*24*, *25*), highlighting the complex physics that is not yet well understood. Moreover, the use of isolated attosecond pulses in these experiments was necessarily accompanied by a broad EUV bandwidth, that then gave rise to an integrated broad-band photoemission feature comprising multiple valence bands (*11*, *13*, *14*). Other recent work used synchrotron sources to measure the final-state linewidths of photoemission from Cu, and found pronounced variations in the ARPES spectra with small changes in photon energy that could not be assigned to a free-electron final state. This work identified the direct transitions and measured very broad linewidths of >3 eV for unoccupied excited final states in the band structure in the 20 to 150 eV photon energy range (*26*).

Here we directly and unambiguously measure the influence of the band structure of a material on the lifetime of photoelectrons. To accomplish this, we use attosecond pulse trains of well-defined harmonics to measure the photoemission time delays for both free-electron final states as well as final states corresponding to the unoccupied bulk bands of the transition metal Ni (111). We distinguish photoelectron lifetimes from individual valence bands and final states in Ni (111), with additional help from selection rules for photoemission for EUV fields with different polarizations (*1*, *27*). Our results show that photoelectrons experience an abrupt delay of ≈ 212 ± 30 attoseconds when the final-state corresponds to an unoccupied excited state in the Ni band structure. This delay corresponds to the lifetime of the excited state, and can be interpreted physically as a variation of the attenuation length of the final-state wavefunction inside the crystal. Therefore, through a direct time-domain measurement of attosecond photoelectron dynamics, our results provide insights into the fundamental concepts of photoelectron lifetime, inelastic mean free path and also group velocity. Moreover, we observe large angle- (momentum-) dependent variations in photoemission time delay, which are directly related to the final-state band dispersion.

The basic principle underlying our experiments is illustrated in Fig. 1A. Linearly polarized high harmonics are focused collinearly with infrared laser pulses (~26 fs, 780 nm) onto an atomically clean Ni (111) surface. The HHG spectra consist of multiple harmonic orders (11th – 41st) spanning from 17 to 66 eV, which are generated using different noble gases (Xe, Kr, Ar and Ne). The corresponding HHG pulse train comprises of EUV bursts of ~200 attoseconds full with half maximum (FWHM) duration within a ~15 fs (FWHM) envelope (*28*) in the time domain. Photoelectrons with sufficiently large momenta along the surface-normal direction escape the surface and are detected by a hemispherical electron analyzer. In the angle-resolved photoelectron spectrum, the same initial Bloch wavepacket is excited to multiple final states with different kinetic energies, manifesting as a ladder of direct photoemission bands, each separated by twice the fundamental photon energy ($\hbar\omega_L$) (Fig. 1B). Laser-assisted photoemission in the presence of the phase-locked infrared (IR) laser field (3×10^{11} W/cm^2) modulates the photoelectron spectra as a function of relative delay between the EUV pump and IR probe fields (τ_d). This allows us to extract photoelectron dynamics on attosecond time scales and Å length scales, by analyzing the attosecond beating due to the interference of two-photon quantum pathways that lead to the same final photoelectron energy (in a technique called RABBITT) (*16*, *28*). It has been shown that RABBITT and attosecond-streaking yield the same temporal information about the photoemission process (*19*, *20*).

We first probed the electronic band structure of Ni (111) by studying the dependence of the static photoelectron spectra on the EUV photon energy and polarization, as shown in Fig. 2A. Dramatic differences can be observed for photoemission excited by s- and p-polarized EUV fields, which can be understood in terms of the selection rules for direct interband transitions (*1*, *27*). Taking these selection rules into account and considering our experimental geometry (45° angle of incidence of the HHG beam), we can unambiguously assign the two photoemission peaks in Fig. 2A that are excited by s-polarized light to the two valence bands with Λ_3 symmetry (Λ_3^α with a binding energy of ~0.6 eV and Λ_3^β ~1.25 eV). The additional spectral weight observed for p-polarized light is from the Λ_1 initial band (~1.7 eV) (see Fig. 2B). Both s- and p-polarized photoemission exhibit peak shifts when excited by different photon energies, which is clear evidence of contributions from bulk-band transitions. Assuming direct transitions to a free-electron-like final state, we can map the electron momentum in the surface-normal direction $\mathbf{k}_\perp$ for different photon energies (*1*, *29*, *30*). The extracted band structure is plotted in Fig. 2B. The good agreement of our photoelectron spectra with previous studies using synchrotron light covering a similar energy range (*30*) (see Fig. 2B) underlines that high harmonics are ideal for capturing electron and band structure dynamics with sub-fs time resolution, good energy resolution (100~300meV), easy manipulation of the photon energy and polarization (*31*), and perfect synchronization to the driving laser. Note that the calculated valence bands using density functional theory (DFT) are ~0.7 eV deeper than experiment, due to strong correlations present for Ni 3*d* electrons (*30*, *32*).

The most pronounced feature of Fig. 2A is the enhancement in the intensity of the low-energy spectral peak (~ -1.25 eV) upon excitation by ~24 eV HHG photons (15th order). This resonant feature clearly appears in the spectra

that emerge from excitation by an s-polarized EUV field, indicating that the Λ_3^β band is the initial band. Considering the band structure of Ni (111) along Γ-L, we can assign this spectral resonance to direct interband transitions from the Λ_3^β initial band to the high-energy unoccupied Λ_1^B final band located at ~24 eV above the Fermi level, as indicated by the blue arrow in Fig. 2B.

In photoemission theory, the matrix element responsible for photoelectron spectra can be written as $M_{fi} = \langle f | H^{int} | i \rangle$, where $|i\rangle$ is the initial state, $|f\rangle$ is the final state and $H^{int} = \mathbf{A}_X \cdot \mathbf{p} + \mathbf{p} \cdot \mathbf{A}_X$ represents the interaction Hamiltonian between an electron and EUV electromagnetic radiation with the vector potential $\mathbf{A}_X$. The final-state wavefunction can be represented as a time-reversed low-energy electron diffraction (LEED) state, composed of a free-electron wave arriving at the detector and a damped Bloch wave inside the crystal (*1*, *33*), with a characteristic damping length directly related to the inelastic mean free path and photoelectron lifetime. The increase in photoemission intensity as a result of this final-state resonance can be attributed to an increase in photoelectron lifetime, with associated elongation of the characteristic damping length of the final-state wavefunction, which strongly enhances the spatial overlap between the initial and final-state wavefunctions - and hence the transition probability. The energy-dependent photoemission intensity of the Λ_3^β band is summarized in Fig. 3B, together with a fit to a Lorentzian function with width γ = 3.68 ± 0.88 eV and centered at 24.40 eV, which is consistent with previous studies (*26*). Thus, the characteristic lifetime of this final state can be extracted from $\tau_{spec} = \hbar/\gamma$ = 179 ± 43 as.

To directly measure the difference in photoelectron lifetimes between electrons excited into high-energy final bands (i.e. on resonance) and those excited into free-electron final states located in the band-gap region (*1*, *33*), we introduced an IR laser field to dress the photoelectrons. In the presence of the dressing laser field, there are two distinct quantum paths from an initial state to the same side-band, namely (i) absorption $\hbar\omega_{2n-1} + \hbar\omega_L$ and (ii) emission $\hbar\omega_{2n+1} - \hbar\omega_L$ of an IR photon (fig. S1B). When the relative time delay τ_d between the HHG pump and the IR probe is changed, the intensity of side bands from a given initial band is modulated as a result of quantum-path interferences (*16*, *28*),

$$S_{2n}(\tau_d) = A_0 \sin\left[2\omega_L(\tau_d - \tau_X - \tau_{PE})\right] \quad (1)$$

where A_0 is the intensity of modulation, $\tau_X = (\phi_{2n+1} - \phi_{2n-1})/2\omega_L$ represents a time delay contributed by the phase chirp between neighboring harmonics ($\phi_{2n+1} - \phi_{2n-1}$) and τ_{PE} is the photoemission delay. Simultaneous measurement of two photoelectron wavepackets excited by the same harmonic orders allows us to cancel the influence of attochirp (τ_X). This method was first implemented and validated for isolated atoms (*16*). In our experiments, we use the non-resonant photoemission from Λ_3^α band as the timing reference, and determine the relative photoemission delay of the resonant $\tau_{PE}(\Lambda_3^\beta) - \tau_{PE}(\Lambda_3^\alpha)$ and non-resonant $\tau_{PE}(\Lambda_1) - \tau_{PE}(\Lambda_3^\alpha)$. This allows us to compare time delays for comparable photoelectron energies, and cancel effects due to the attochirp or field-induced phase delays.

We first measured the time delay $\tau_{PE}(\Lambda_3^\beta) - \tau_{PE}(\Lambda_3^\alpha)$ using s-polarized HHG fields. In Fig. 3C, we plot a set of experimental RABBITT interferograms for τ_d in range of -2 to 2 fs. The interferograms were obtained by integrating the photoelectron spectra over ±2.5° around the Γ point and subtracting the background spectrum obtained well before time-zero. We intentionally selected a small angular region in the analysis to avoid the ambiguities resulting from angle-dependent photoemission time delay (see below). Figure 3C clearly shows that photoelectrons from the Λ_3^β band are significantly delayed for sideband (SB) 16 (corresponding to a photon energy 25.6 eV), which manifests as a large offset in oscillations in the interferograms. This time delay gradually vanishes at increasing and decreasing photon energies, showing a non-monotonic change of $\tau_{PE}(\Lambda_3^\beta) - \tau_{PE}(\Lambda_3^\alpha)$ as a function of photon energies. One-dimensional (1D) lineouts corresponding to the Λ_3^α and Λ_3^β bands in the side-band region are extracted in the panel on the right side of Fig. 3C, making it possible to determine the precise values of $\tau_{PE}(\Lambda_3^\beta) - \tau_{PE}(\Lambda_3^\alpha)$ as a function of energy. The results are summarized in Fig. 3A (see supplementary materials for detailed analysis). By comparing this relative photoemission delay with the spectral resonance (Fig. 3B), we find that the observed maximum in time delay coincides with the spectral resonance at the same photon energy, strongly indicating that the observed photoemission time delay originates from the excited-state band structure of Ni (111). Most importantly, the time delay measured using laser-assisted photoemission, τ_{chron} = 212 ± 30 as, agrees with τ_{spec} = 179 ± 43 as from the spectral resonance, within error bars.

To extract the photoemission time delay $\tau_{PE}(\Lambda_1) - \tau_{PE}(\Lambda_3^\alpha)$, we used p-polarized EUV fields for photoemission (Fig. 1C). We note that in this situation, the low-energy side-band intensity of the RABBITT oscillations has contributions from both Λ_1 and Λ_3^β bands. With the knowledge of the intensity contributions from these two initial bands, the time delay $\tau_{PE}(\Lambda_1) - \tau_{PE}(\Lambda_3^\alpha)$ can be extracted (see supplementary materials), as shown in Fig. 3A. In strong contrast to the Λ_3^β band, photoemission from the

Λ_1 band exhibits a very small time delay relative to that from the Λ_3^α band and varies smoothly across the photon energy range.

In photoemission theory, the photoelectron lifetime can be understood as the time taken for the wavefunction to evolve from a Bloch wave inside the material into a free-electron wavefunction outside the solid. Semi-classically, this is also the time the photoelectron spends moving a distance corresponding to an inelastic mean free path (IMFP) (*33*, *34*). As we will show below, the on-resonance time delay measured in our experiments can be directly related to the lifetime of the final state high-energy band. The fact that our measured time delay agrees well with the lifetime extracted from the spectral linewidth indicates that the lifetimes of photoelectrons originating from the initial Λ_3^α band are very small (within experimental error ~ ±53 as). At the same time, the photoelectron lifetimes corresponding to the Λ_1 band are ≈50 as longer (Fig. 3A). Since both bands exhibit a smooth variation in photoemission cross section over the photon energy range used here (see supplementary materials), it is reasonable to assume their photoelectron lifetimes are slowly varying as a function of photon energies. Thus, the results presented in Fig. 3A can be interpreted as an abrupt increase of ~212 as in photoelectron lifetime from the Λ_3^β band when the direct transition approaches a bulk final band (Λ_1^B), resulting in a final-state resonance.

To physically interpret our measurements, we employed a 1D semiclassical model (*35*) to calculate the RABBITT interferograms of photoelectrons with a same final energy, but emitted from different depths (e.g. 2 Å and 10 Å) below the surface to simulate photoelectrons with different IMFPs. This model considers the quantum phases accumulated as the photoelectrons scatter from the IR dressing field and crystal potential (see supplementary materials). The IR dressing field inside the metal is mostly screened (see supplementary materials and inset of Fig. 3D) and has negligible influence on photoelectrons as they travel to the surface (*36*). One dimensional lineouts of the RABBITT oscillations are plotted in Fig. 3D for photoelectrons with a free-electron velocity corresponding to an energy of 25.5 eV inside the crystal. We find the RABBITT oscillation traces of photoelectrons emitted 10 Å below the surface are delayed by 267 attoseconds compared to those corresponding to photoelectrons originating 2 Å below the surface, which is consistent with the measured lifetime difference between them. This allows us to directly relate our time-domain measurements to the lifetimes and inelastic mean free paths of photoelectrons, which determines the surface and bulk contributions (*1*, *33*). To determine the inelastic mean free path, a remaining question is which photoelectron velocity should be used to calculate the inelastic mean free path? In a periodic crystal lattice, the elastic interaction with atoms strongly modifies the electron energy-momentum relationship, giving rise to the electronic band structure. It is generally believed that the velocity of photoelectrons can be represented by the group velocity of the corresponding final bands, which is given by the derivative of the energy with respect to the momentum wave-vector $\mathbf{k}_\perp$ (*11*, *13*, *14*)**.** To determine the final-state group velocity, we employed an *ab-initio* calculation for the bulk band-structure of Ni along Γ-L, including the high-energy valence bands (~24 eV). We find the final band involved in the resonant transition (highlighted in Fig. 2B) has a narrow bandwidth (~4 eV), consistent with our experimental spectra. The corresponding group velocity is given by $\partial E_f/\partial(\hbar\mathbf{k}_\perp) \approx 3.0$ eVÅ/ħ, and is significantly smaller than the velocity of a free electron with the same kinetic energy (~19.1 eVÅ/ħ). Using the calculated group velocity, we obtain an inelastic mean free path of at most 1 Å, which is much smaller than values reported in other studies (*37*, *38*). We believe this discrepancy arises because the group velocity is not the transport velocity for high-energy photoelectrons. As pointed out in previous studies (*34*), high energy (>20 eV) photoelectrons leave the crystal before they feel the influence of the crystal lattice, so they behave more like plane waves with a free-electron dispersion**.** By using the corresponding free-electron velocity in our analysis, we extract a IMFP of ~6 Å for photoelectrons that are emitted on resonance, consistent with previous studies (*29*). In contrast, the inelastic mean free paths of photoelectrons from the Λ_3^α and Λ_1 bands, as well as those from the Λ_3^β band away from the spectral resonance, are estimated to be approximately 3 Å, manifesting their surface-emission nature.

Other important evidence that the band structure of the material strongly influences the photoemission lifetime can be seen from the angle-dependence of the lifetime as a function of electron transverse momentum $\mathbf{k}_{//}$. To cancel any time delays imposed by the incident and reflected laser fields (*35*, *36*) and to extract the contribution due to band-structure effects, the RABBITT oscillations from the Λ_3^α band were used as the timing reference at different emission angles (Θ) for each side band (see supplementary materials). The angle-dependent results of $\tau_{PE}\left(\Lambda_3^\beta,\theta\right)-\tau_{PE}\left(\Lambda_3^\alpha,\theta\right)$ are summarized in Fig. 4A for SB16 and SB14 (near the resonance). As shown in Fig. 4A, the time delay $\tau_{PE}\left(\Lambda_3^\beta,\theta\right)-\tau_{PE}\left(\Lambda_3^\alpha,\theta\right)$ at SB 16 reaches its maximum value ~220 as at $\bar{\Gamma}$ point (Θ = 0), while it reduces to ~30 as when the emission angle approaches Θ = ±15°. The overall trend is symmetric around the $\bar{\Gamma}$ point, which strongly suggests the band-structure origin of this angle-dependent photoemission time delay. Most interestingly, $\tau_{PE}\left(\Lambda_3^\beta,\theta\right)-\tau_{PE}\left(\Lambda_3^\alpha,\theta\right)$

exhibits a double-peak shape at SB 14 (Fig. 4A), as the time delay increases to its maximum on-resonance value at $\theta \approx \pm 6°$ and then decreases for larger emission angles.

To quantitatively interpret this angle-dependent photoemission lifetime, we compare the predicted time delays associated with our model and DFT calculations (see supplementary materials) with the experimental data, as shown in Fig. 4A. Our results show that for SB 16, the HHG photon energy closely matches the resonant excited state at the $\bar{\Gamma}$ point, yielding a maximum time delay for $\theta = 0$. Moreover, the time delay monotonically decreases at larger emission angles, since final-state band dispersion causes the transition to be off resonance. On the other hand, for SB 14 where the photon energy is ~3.2 eV lower, the resonant transition is not accessible at the $\bar{\Gamma}$ point, but is on resonance and yields a maximum time delay at a ~ 6° emission angle (Fig. 4C). The key factor for this agreement is the dispersion of the Σ_1 final band (~ -14 eVÅ/$\hbar$), which determines the slope of the time delay as a function of θ.

Our results highlight the importance of the material band structure on photoemission time delays, which must also be taken into account even at higher photon energies. In future, this approach can be used to experimentally access quasiparticle lifetimes, electron mean free paths, electron-electron scattering and dynamical screening, all of which represent grand challenges for condensed matter theory. Moreover, other effects, including Cooper minima (*39*) and Fano resonances (*40*), could also lead to significant delays, making attosecond studies of metal valence bands a challenging, but also rich and interesting, problem.

REFERENCES AND NOTES

1. S. Hüfner, *Photoelectron Spectroscopy: Principles and Applications* (Springer-Verlag, ed. 3, 2003).
2. F. Schmitt, P. S. Kirchmann, U. Bovensiepen, R. G. Moore, L. Rettig, M. Krenz, J.-H. Chu, N. Ru, L. Perfetti, D. H. Lu, M. Wolf, I. R. Fisher, Z.-X. Shen, Transient electronic structure and melting of a charge density wave in $TbTe_3$. *Science* **321**, 1649–1652 (2008). Medline doi:10.1126/science.1160778
3. A. Rundquist, C. G. Durfee 3rd, Z. Chang, C. Herne, S. Backus, M. M. Murnane, H. C. Kapteyn, Phase-matched generation of coherent soft X-rays. *Science* **280**, 1412–1415 (1998). Medline doi:10.1126/science.280.5368.1412
4. D. Popmintchev, C. Hernández-García, F. Dollar, C. Mancuso, J. A. Pérez-Hernández, M.-C. Chen, A. Hankla, X. Gao, B. Shim, A. L. Gaeta, M. Tarazkar, D. A. Romanov, R. J. Levis, J. A. Gaffney, M. Foord, S. B. Libby, A. Jaron-Becker, A. Becker, L. Plaja, M. M. Murnane, H. C. Kapteyn, T. Popmintchev, Ultraviolet surprise: Efficient soft x-ray high-harmonic generation in multiply ionized plasmas. *Science* **350**, 1225–1231 (2015). Medline doi:10.1126/science.aac9755
5. S. Hellmann, T. Rohwer, M. Kalläne, K. Hanff, C. Sohrt, A. Stange, A. Carr, M. M. Murnane, H. C. Kapteyn, L. Kipp, M. Bauer, K. Rossnagel, Time-domain classification of charge-density-wave insulators. *Nat. Commun.* **3**, 1069 (2012). Medline doi:10.1038/ncomms2078
6. S. Eich, A. Stange, A. V. Carr, J. Urbancic, T. Popmintchev, M. Wiesenmayer, K. Jansen, A. Ruffing, S. Jakobs, T. Rohwer, S. Hellmann, C. Chen, P. Matyba, L. Kipp, K. Rossnagel, M. Bauer, M. M. Murnane, H. C. Kapteyn, S. Mathias, M. Aeschlimann, Time- and angle-resolved photoemission spectroscopy with optimized high-harmonic pulses using frequency-doubled Ti:sapphire lasers. *J. Electron Spectrosc. Relat. Phenom.* **195**, 231–236 (2014). doi:10.1016/j.elspec.2014.04.013
7. W. Li, A. A. Jaroń-Becker, C. W. Hogle, V. Sharma, X. Zhou, A. Becker, H. C. Kapteyn, M. M. Murnane, Visualizing electron rearrangement in space and time during the transition from a molecule to atoms. *Proc. Natl. Acad. Sci. U.S.A.* **107**, 20219–20222 (2010). Medline doi:10.1073/pnas.1014723107
8. S. Mathias, C. La-O-Vorakiat, P. Grychtol, P. Granitzka, E. Turgut, J. M. Shaw, R. Adam, H. T. Nembach, M. E. Siemens, S. Eich, C. M. Schneider, T. J. Silva, M. Aeschlimann, M. M. Murnane, H. C. Kapteyn, Probing the timescale of the exchange interaction in a ferromagnetic alloy. *Proc. Natl. Acad. Sci. U.S.A.* **109**, 4792–4797 (2012). Medline doi:10.1073/pnas.1201371109
9. E. Turgut, C. La-o-Vorakiat, J. M. Shaw, P. Grychtol, H. T. Nembach, D. Rudolf, R. Adam, M. Aeschlimann, C. M. Schneider, T. J. Silva, M. M. Murnane, H. C. Kapteyn, S. Mathias, Controlling the competition between optically induced ultrafast spin-flip scattering and spin transport in magnetic multilayers. *Phys. Rev. Lett.* **110**, 197201 (2013). Medline doi:10.1103/PhysRevLett.110.197201
10. L. Miaja-Avila, G. Saathoff, S. Mathias, J. Yin, C. La-o-vorakiat, M. Bauer, M. Aeschlimann, M. M. Murnane, H. C. Kapteyn, Direct measurement of core-level relaxation dynamics on a surface-adsorbate system. *Phys. Rev. Lett.* **101**, 046101 (2008). Medline doi:10.1103/PhysRevLett.101.046101
11. A. L. Cavalieri, N. Müller, T. Uphues, V. S. Yakovlev, A. Baltuška, B. Horvath, B. Schmidt, L. Blümel, R. Holzwarth, S. Hendel, M. Drescher, U. Kleineberg, P. M. Echenique, R. Kienberger, F. Krausz, U. Heinzmann, Attosecond spectroscopy in condensed matter. *Nature* **449**, 1029–1032 (2007). Medline doi:10.1038/nature06229
12. R. Locher, L. Castiglioni, M. Lucchini, M. Greif, L. Gallmann, J. Osterwalder, M. Hengsberger, U. Keller, Energy-dependent photoemission delays from noble metal surfaces by attosecond interferometry. *Optica* **2**, 405–410 (2015). doi:10.1364/OPTICA.2.000405
13. S. Neppl, R. Ernstorfer, E. M. Bothschafter, A. L. Cavalieri, D. Menzel, J. V. Barth, F. Krausz, R. Kienberger, P. Feulner, Attosecond time-resolved photoemission from core and valence states of magnesium. *Phys. Rev. Lett.* **109**, 087401 (2012). Medline doi:10.1103/PhysRevLett.109.087401
14. S. Neppl, R. Ernstorfer, A. L. Cavalieri, C. Lemell, G. Wachter, E. Magerl, E. M. Bothschafter, M. Jobst, M. Hofstetter, U. Kleineberg, J. V. Barth, D. Menzel, J. Burgdörfer, P. Feulner, F. Krausz, R. Kienberger, Direct observation of electron propagation and dielectric screening on the atomic length scale. *Nature* **517**, 342–346 (2015). Medline doi:10.1038/nature14094
15. R. Pazourek, S. Nagele, J. Burgdörfer, Attosecond chronoscopy of photoemission. *Rev. Mod. Phys.* **87**, 765–802 (2015). doi:10.1103/RevModPhys.87.765
16. K. Klünder, J. M. Dahlström, M. Gisselbrecht, T. Fordell, M. Swoboda, D. Guénot, P. Johnsson, J. Caillat, J. Mauritsson, A. Maquet, R. Taïeb, A. L'Huillier, Probing single-photon ionization on the attosecond time scale. *Phys. Rev. Lett.* **106**, 143002 (2011). Medline doi:10.1103/PhysRevLett.106.143002
17. M. Schultze, M. Fiess, N. Karpowicz, J. Gagnon, M. Korbman, M. Hofstetter, S. Neppl, A. L. Cavalieri, Y. Komninos, T. Mercouris, C. A. Nicolaides, R. Pazourek, S. Nagele, J. Feist, J. Burgdörfer, A. M. Azzeer, R. Ernstorfer, R. Kienberger, U. Kleineberg, E. Goulielmakis, F. Krausz, V. S. Yakovlev, Delay in photoemission. *Science* **328**, 1658–1662 (2010). Medline doi:10.1126/science.1189401
18. L. Miaja-Avila, C. Lei, M. Aeschlimann, J. L. Gland, M. M. Murnane, H. C. Kapteyn, G. Saathoff, Laser-assisted photoelectric effect from surfaces. *Phys. Rev. Lett.* **97**, 113604 (2006). Medline doi:10.1103/PhysRevLett.97.113604
19. C.-H. Zhang, U. Thumm, Electron-ion interaction effects in attosecond time-resolved photoelectron spectra. *Phys. Rev. A* **82**, 043405 (2010). doi:10.1103/PhysRevA.82.043405
20. J. M. Dahlström, D. Guénot, K. Klünder, M. Gisselbrecht, J. Mauritsson, A. L'Huillier, A. Maquet, R. Taïeb, Theory of attosecond delays in laser-assisted photoionization. *Chem. Phys.* **414**, 53–64 (2013). doi:10.1016/j.chemphys.2012.01.017
21. C.-H. Zhang, U. Thumm, Attosecond photoelectron spectroscopy of metal surfaces. *Phys. Rev. Lett.* **102**, 123601 (2009). Medline doi:10.1103/PhysRevLett.102.123601
22. C. Lemell, B. Solleder, K. Tokési, J. Burgdörfer, Simulation of attosecond streaking of electrons emitted from a tungsten surface. *Phys. Rev. A* **79**, 062901 (2009). doi:10.1103/PhysRevA.79.062901

23. A. K. Kazansky, P. M. Echenique, One-electron model for the electronic response of metal surfaces to subfemtosecond photoexcitation. *Phys. Rev. Lett.* **102**, 177401 (2009). Medline doi:10.1103/PhysRevLett.102.177401
24. E. E. Krasovskii, Attosecond spectroscopy of solids: Streaking phase shift due to lattice scattering. *Phys. Rev. B* **84**, 195106 (2011). doi:10.1103/PhysRevB.84.195106
25. A. G. Borisov, D. Sánchez-Portal, A. K. Kazansky, P. M. Echenique, Resonant and nonresonant processes in attosecond streaking from metals. *Phys. Rev. B* **87**, 121110(R) (2013). doi:10.1103/PhysRevB.87.121110
26. F. Roth, C. Lupulescu, E. Darlatt, A. Gottwald, W. Eberhardt, Angle resolved photoemission from Cu single crystals: Known facts and a few surprises about the photoemission process. *J. Electron Spectrosc. Relat. Phenom.* 10.1016/j.elspec.2015.09.006 (2015).
27. J. Hermanson, Final-state symmetry and polarization effects in angle-resolved photoemission spectroscopy. *Solid State Commun.* **22**, 9–11 (1977). doi:10.1016/0038-1098(77)90931-0
28. P. M. Paul, E. S. Toma, P. Breger, G. Mullot, F. Augé, P. Balcou, H. G. Muller, P. Agostini, Observation of a train of attosecond pulses from high harmonic generation. *Science* **292**, 1689–1692 (2001). Medline doi:10.1126/science.1059413
29. J. A. Knapp, F. J. Himpsel, D. E. Eastman, Experimental energy band dispersions and lifetimes for valence and conduction bands of copper using angle-resolved photoemissoin. *Phys. Rev. B* **19**, 4952–4964 (1979). doi:10.1103/PhysRevB.19.4952
30. F. J. Himpsel, J. A. Knapp, D. E. Eastman, Experimental energy-band dispersions and exchange splitting for Ni. *Phys. Rev. B* **19**, 2919–2927 (1979). doi:10.1103/PhysRevB.19.2919
31. C. Chen, Z. Tao, C. Hernández-García, P. Matyba, A. Carr, R. Knut, O. Kfir, D. Zusin, C. Gentry, P. Grychtol, O. Cohen, L. Plaja, A. Becker, A. Jaron-Becker, H. Kapteyn, M. Murnane, Tomographic reconstruction of circularly polarized high-harmonic fields: 3D attosecond metrology. *Sci. Adv.* **2**, e1501333 (2016). Medline doi:10.1126/sciadv.1501333
32. A. Liebsch, Effect of self-energy corrections on the valence-band photoemission spectra of Ni. *Phys. Rev. Lett.* **43**, 1431–1434 (1979). doi:10.1103/PhysRevLett.43.1431
33. B. Feuerbacher, R. F. Willis, Photoemission and electron states at clean surfaces. *J. Phys. C* **9**, 169–216 (1976). doi:10.1088/0022-3719/9/2/007
34. J. S. Dolado, V. M. Silkin, M. A. Cazalilla, A. Rubio, P. M. Echenique, Lifetimes and mean-free paths of hot electrons in the alkali metals. *Phys. Rev. B* **64**, 195128 (2001). doi:10.1103/PhysRevB.64.195128
35. M. Lucchini, A. Ludwig, L. Kasmi, L. Gallmann, U. Keller, Semi-classical approach to compute RABBITT traces in multi-dimensional complex field distributions. *Opt. Express* **23**, 8867–8879 (2015). Medline doi:10.1364/OE.23.008867
36. M. Lucchini, L. Castiglioni, L. Kasmi, P. Kliuiev, A. Ludwig, M. Greif, J. Osterwalder, M. Hengsberger, L. Gallmann, U. Keller, Light-matter interaction at surfaces in the spatiotemporal limit of macroscopic models. *Phys. Rev. Lett.* **115**, 137401 (2015). Medline doi:10.1103/PhysRevLett.115.137401
37. C. J. Powell, Attenuation lengths of low-energy electrons in solids. *Surf. Sci.* **44**, 29–46 (1974). doi:10.1016/0039-6028(74)90091-0
38. D. E. Eastman, J. A. Knapp, F. J. Himpsel, Direct determination of lifetime and energy dispersion for the empty Δ_1 conduction band of copper. *Phys. Rev. Lett.* **41**, 825–828 (1978). doi:10.1103/PhysRevLett.41.825
39. G. Rossi, I. Lindau, L. Braicovich, I. Abbati, Cooper-minimum effects in the photoionization cross sections of 4*d* and 5*d* electrons in solid compounds. *Phys. Rev. B* **28**, 3031–3042 (1983). doi:10.1103/PhysRevB.28.3031
40. C. Guillot, Y. Ballu, J. Paigné, J. Lecante, K. P. Jain, P. Thiry, R. Pinchaux, Y. Pétroff, L. M. Falicov, Resonant photoemission in nickel metal. *Phys. Rev. Lett.* **39**, 1632–1635 (1977). doi:10.1103/PhysRevLett.39.1632
41. D. L. Miller, M. W. Keller, J. M. Shaw, A. N. Chiaramonti, R. R. Keller, Epitaxial (111) films of Cu, Ni, and Cu_xNi_y on α-Al_2O_3 (0001) for graphene growth by chemical vapor deposition. *J. Appl. Phys.* **112**, 064317 (2012). doi:10.1063/1.4754013
42. Certain commercial instruments are identified to specify the experimental study adequately. This does not imply endorsement by NIST or that the instruments are the best available for the purpose.
43. D. E. Eastman, F. J. Himpsel, J. A. Knapp, Experimental band structure and temperature-dependent magnetic exchange splitting of nickel using angle-resolved photoemission. *Phys. Rev. Lett.* **40**, 1514–1517 (1978). doi:10.1103/PhysRevLett.40.1514
44. G. Kresse, J. Furthmüller, Efficiency of ab-initio total energy calculations for metals and semiconductors using a plane-wave basis set. *Comput. Mater. Sci.* **6**, 15–50 (1996). doi:10.1016/0927-0256(96)00008-0
45. G. Kresse, J. Furthmüller, Efficient iterative schemes for *ab initio* total-energy calculations using a plane-wave basis set. *Phys. Rev. B* **54**, 11169–11186 (1996). Medline doi:10.1103/PhysRevB.54.11169
46. G. Kresse, D. Joubert, From ultrasoft pseudopotentials to the projector augmented-wave method. *Phys. Rev. B* **59**, 1758–1775 (1999). doi:10.1103/PhysRevB.59.1758
47. P. E. Blöchl, Projector augmented-wave method. *Phys. Rev. B* **50**, 17953–17979 (1994). Medline doi:10.1103/PhysRevB.50.17953
48. J. P. Perdew, Y. Wang, Accurate and simple analytic representation of the electron-gas correlation energy. *Phys. Rev. B* **45**, 13244–13249 (1992). Medline doi:10.1103/PhysRevB.45.13244
49. P. Matyba, A. Carr, C. Chen, D. L. Miller, G. Peng, S. Mathias, M. Mavrikakis, D. S. Dessau, M. W. Keller, H. C. Kapteyn, M. Murnane, Controlling the electronic structure of graphene using surface-adsorbate interactions. *Phys. Rev. B* **92**, 041407(R) (2015). doi:10.1103/PhysRevB.92.041407
50. M. Hasegawa, K. Nishidate, T. Hosokai, N. Yoshimoto, Electronic-structure modification of graphene on Ni (111) surface by the intercalation of a noble metal. *Phys. Rev. B* **87**, 085439 (2013). doi:10.1103/PhysRevB.87.085439
51. J. Lobo-Checa, T. Okuda, M. Hengsberger, L. Patthey, T. Greber, P. Blaha, J. Osterwalder, Hidden surface states on pristine and H-passivated Ni (111): Angle-resolved photoemission and density-functional calculations. *Phys. Rev. B* **77**, 075415 (2008). doi:10.1103/PhysRevB.77.075415
52. H. J. Monkhorst, J. D. Pack, Special points for Brillouin-zone integrations. *Phys. Rev. B* **13**, 5188–5192 (1976). doi:10.1103/PhysRevB.13.5188
53. M. Methfessel, A. T. Paxton, High-precision sampling for Brillouin-zone integration in metals. *Phys. Rev. B* **40**, 3616–3621 (1989). Medline doi:10.1103/PhysRevB.40.3616
54. W. M. Haynes, *CRC Handbook of Chemistry and Physics* (CRC Press/Taylor and Francis, ed. 94, 2014).
55. V. L. Moruzzi, J. F. Janak, A. B. Williams, *Calculated Electronic Properties of Metals* (Pergamon, 1978).
56. H. Eckardt, L. Fritsche, The effect of electron correlations and finite temperatures on the electronic structure of ferromagnetic nickel. *J. Phys. F* **17**, 925–941 (1987). doi:10.1088/0305-4608/17/4/020
57. F. Manghi, V. Bellini, J. Osterwalder, T. J. Kreutz, P. Aebi, C. Arcangeli, Correlation effects in the low-energy region of nickel photoemission spectra. *Phys. Rev. B* **59**, R10409 (1999). doi:10.1103/PhysRevB.59.R10409
58. J. P. Perdew, K. Burke, M. Ernzerhof, Generalized gradient approximation made simple. *Phys. Rev. Lett.* **77**, 3865–3868 (1996). Medline doi:10.1103/PhysRevLett.77.3865
59. D. Vanderbilt, Soft self-consistent pseudopotentials in a generalized eigenvalue formalism. *Phys. Rev. B* **41**, 7892(R) (1990). doi:10.1103/PhysRevB.41.7892
60. P. Giannozzi, S. Baroni, N. Bonini, M. Calandra, R. Car, C. Cavazzoni, D. Ceresoli, G. L. Chiarotti, M. Cococcioni, I. Dabo, A. Dal Corso, S. de Gironcoli, S. Fabris, G. Fratesi, R. Gebauer, U. Gerstmann, C. Gougoussis, A. Kokalj, M. Lazzeri, L. Martin-Samos, N. Marzari, F. Mauri, R. Mazzarello, S. Paolini, A. Pasquarello, L. Paulatto, C. Sbraccia, S. Scandolo, G. Sclauzero, A. P. Seitsonen, A. Smogunov, P. Umari, R. M. Wentzcovitch, QUANTUM ESPRESSO: A modular and open-source software project for quantum simulations of materials. *J. Phys. Condens. Matter* **21**, 395502 (2009). Medline doi:10.1088/0953-8984/21/39/395502
61. D. A. Shirley, High-resolution x-ray photoemission spectrum of the valence bands of gold. *Phys. Rev. B* **5**, 4709–4714 (1972). doi:10.1103/PhysRevB.5.4709
62. Y. Mairesse, F. Quéré, Frequency-resolved optical gating for complete reconstruction of attosecond bursts. *Phys. Rev. A* **71**, 011401(R) (2005). doi:10.1103/PhysRevA.71.011401
63. Q. Liao, U. Thumm, Initial-state, mean-free-path, and skin-depth dependence of attosecond time-resolved IR-streaked XUV photoemission from single-crystalline magnesium. *Phys. Rev. A* **89**, 033849 (2014). doi:10.1103/PhysRevA.89.033849

64. K. L. Kliewer, Electromagnetic effects at metal surfaces; A nonlocal view. *Surf. Sci.* **101**, 57–83 (1980). doi:10.1016/0039-6028(80)90599-3
65. A. D. Rakić, A. B. Djurišić, J. M. Elazar, M. L. Majewski, Optical properties of metallic films for vertical-cavity optoelectronic devices. *Appl. Opt.* **37**, 5271–5283 (1998). Medline doi:10.1364/AO.37.005271
66. A. T. Georges, Calculation of surface electromagnetic fields in laser- metal surface interaction. *Opt. Commun.* **188**, 321–331 (2001). doi:10.1016/S0030-4018(00)01173-1
67. E. V. Chulkov, V. M. Silkin, P. M. Echenique, Image potential states on metal surfaces : Binding energies and wave functions. *Surf. Sci.* **437**, 330–352 (1999). doi:10.1016/S0039-6028(99)00668-8
68. N. Armbrust, J. Gudde, U. Höfer, Formation of image-potential states at the graphene/metal interface. *New J. Phys.* **17**, 103043 (2015). doi:10.1088/1367-2630/17/10/103043
69. I. Lindau, P. Pianetta, K. Y. Yu, W. E. Spicer, Photoemission of gold in the energy range 30-300 eV using synchrotron radiation. *Phys. Rev. B* **13**, 492–495 (1976). doi:10.1103/PhysRevB.13.492
70. J. Stöhr, G. Apai, P. S. Wehner, F. R. McFeely, R. S. Williams, D. A. Shirley, Angle-resolved photoemission from valence bands of Cu and Au single crystals using 32-200 eV synchrotron radiation. *Phys. Rev. B* **14**, 5144–5155 (1976). doi:10.1103/PhysRevB.14.5144
71. J. Stöhr, P. S. Wehner, R. S. Williams, G. Apai, D. A. Shirley, Bulk versus surface effects in normal photoemission from Cu (110) in the range $32<h\nu<160$ eV. *Phys. Rev. B* **17**, 587–590 (1978). doi:10.1103/PhysRevB.17.587
72. T.-C. Chiang, J. A. Knapp, M. Aono, D. E. Eastman, Angle-resolved photoemission, valence band dispersions E (k), and electron and hole lifetimes for GaAs. *Phys. Rev. B* **21**, 3513–3522 (1980). doi:10.1103/PhysRevB.21.3513

ACKNOWLEDGMENTS

We thank G. D. Mahan, G. B. Arnold, G. F. Mancini and H. X. Li for helpful discussions. This work was done at JILA. The authors gratefully acknowledge support from the National Science Foundation through the Physics Frontiers Centers Program and the Gordon and Betty Moore Foundation EPiQS Award. T. S. and M. Ma. gratefully acknowledge support from Air Force Office of Scientific Research under a Basic Research Initiative grant (AFOSR FA9550-12-1-0481) and DOE-BES, the Division of Chemical Sciences (grant DE-FG02-05ER15731). The authors declare that they have no competing interests. H.K. and M. Mu have a financial interest in a laser company, KMLabs.

SUPPLEMENTARY MATERIALS

www.sciencemag.org/cgi/content/full/science.aaf6793/DC1
Supplementary Text
Figs. S1 to S9
References (*41*–*72*)

13 March 2016; accepted 11 May 2016
Published online 2 June 2016
10.1126/science.aaf6793

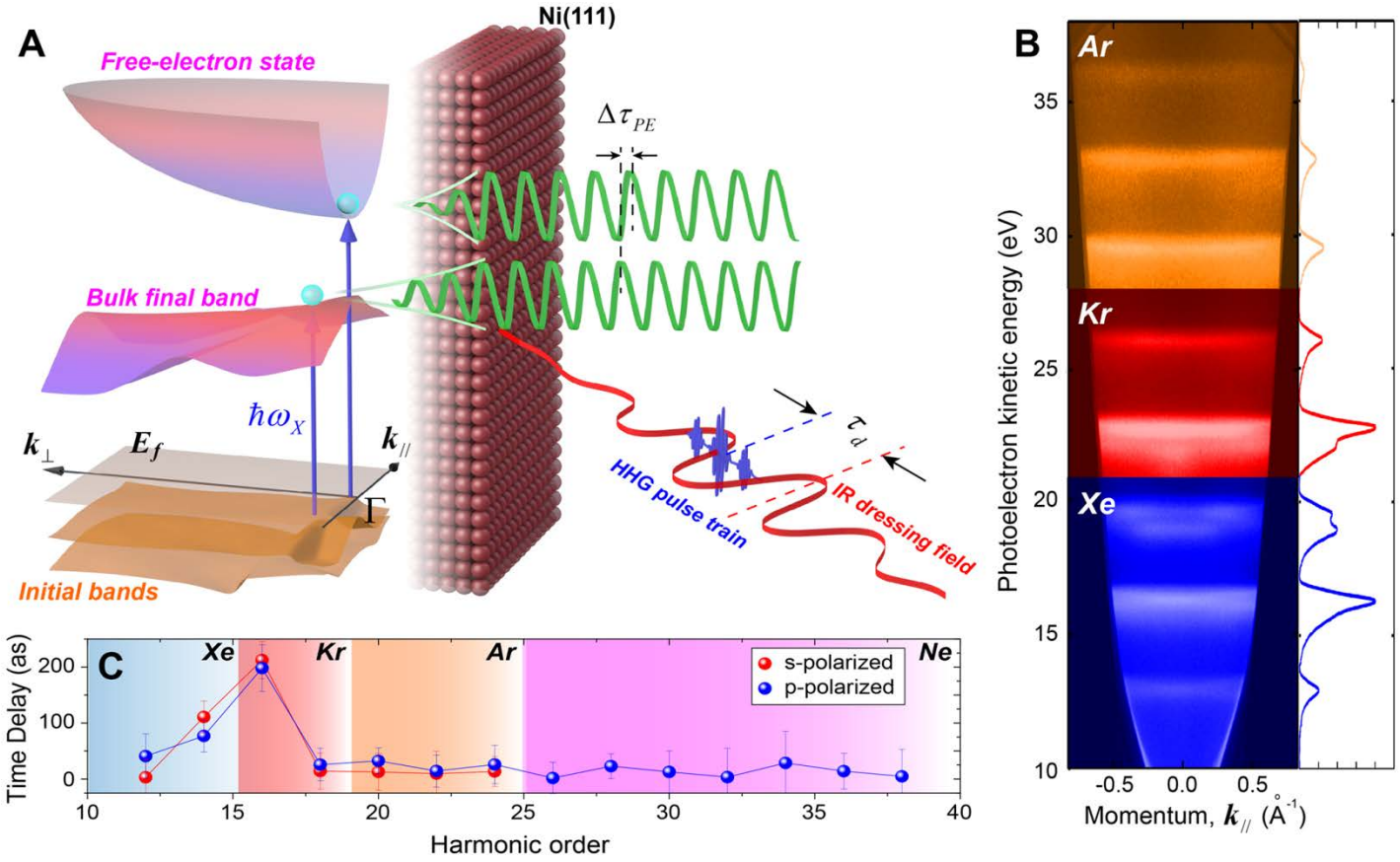

Fig. 1. Photoemission time delay on and off a resonance in the band structure. (**A**) Using high-order harmonics, different photoelectron final states can be accessed, corresponding to free-electron-like states or excited states in the band structure. The damping length of the final-state wavefunction inside the crystal is significantly increased when the transition coincides with a final-state resonance. (**B**) Static ARPES excited by s-polarized HHG. The energy resolution is ~0.3 eV, which is sufficient to distinguish photoemissions from two initial bands (Λ_3^α and Λ_3^β). (**C**) Photoemission time delays from laser-dressed harmonic sidebands for s- and p-polarized HHG for noble gas targets. A significant delay is introduced at side band 16, due to the > 200 attosecond lifetime of the excited-state in the material band structure.

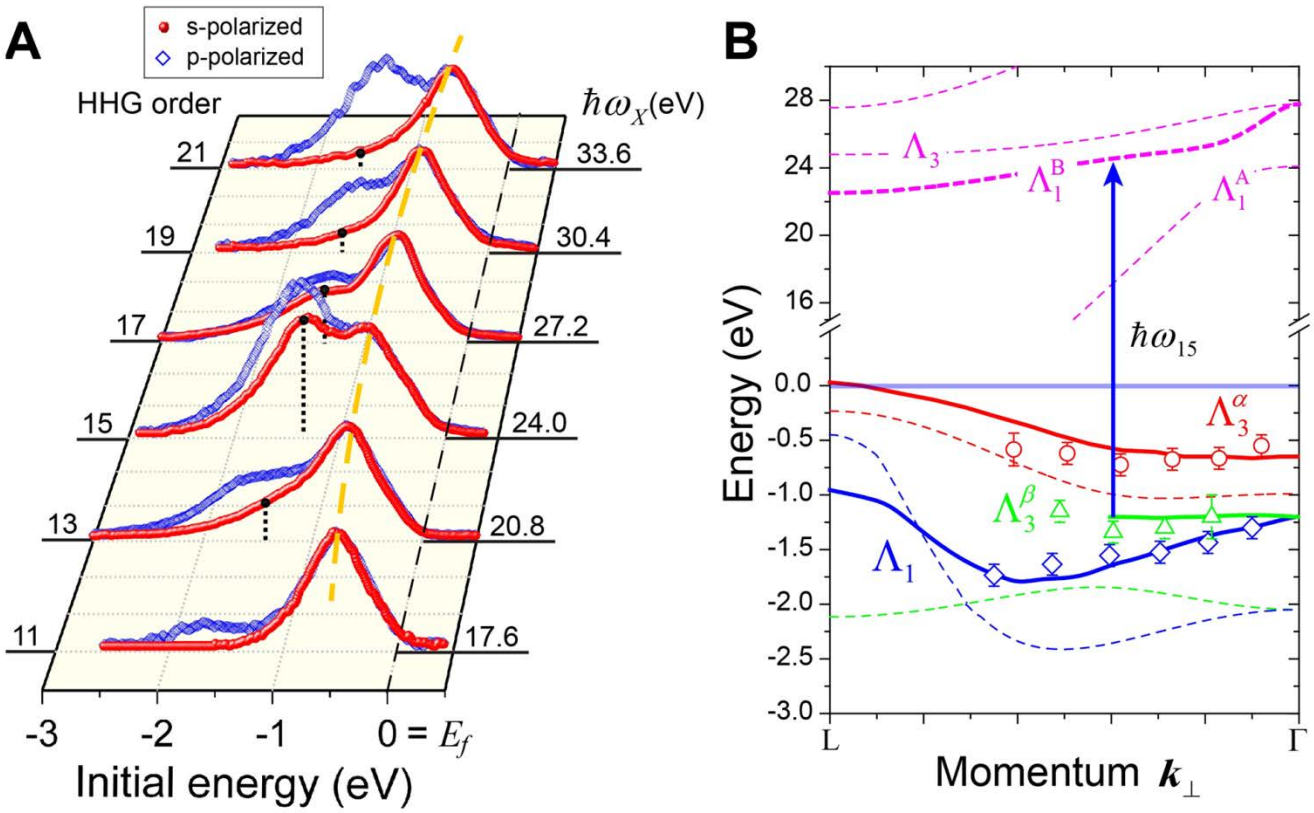

Fig. 2. Final-state resonance in photoemission from Ni (111). (**A**) EDC curves excited by s- (red) and p-polarized (blue) HHG in a normal emission geometry (integrated ~ ±2° around the Γ point). The position of the Fermi level (black dashed line) is determined from the laser photon energy (~1.6 eV) and analyzer work function (4.25 eV). The orange dashed line shows the shift of the high-energy peak with HHG photon energy, underlining the contribution of bulk-band transitions. The intensity of the Λ_3^β band clearly shows a spectral resonance at ~24 eV. (**B**) Band structure along Γ-L (normal to surface) extracted from our data (open symbols) compared to previous experiments (*30*) (solid lines) and DFT calculations (dashed lines). A free-electron final-state in a constant inner potential (*30*) is assumed and used to map the electron momentum normal to the sample surface $\mathbf{k}_\perp$. The final state resonance observed in (A) is highlighted as direct transition from the Λ_3^β initial band to the Λ_1^B final band.

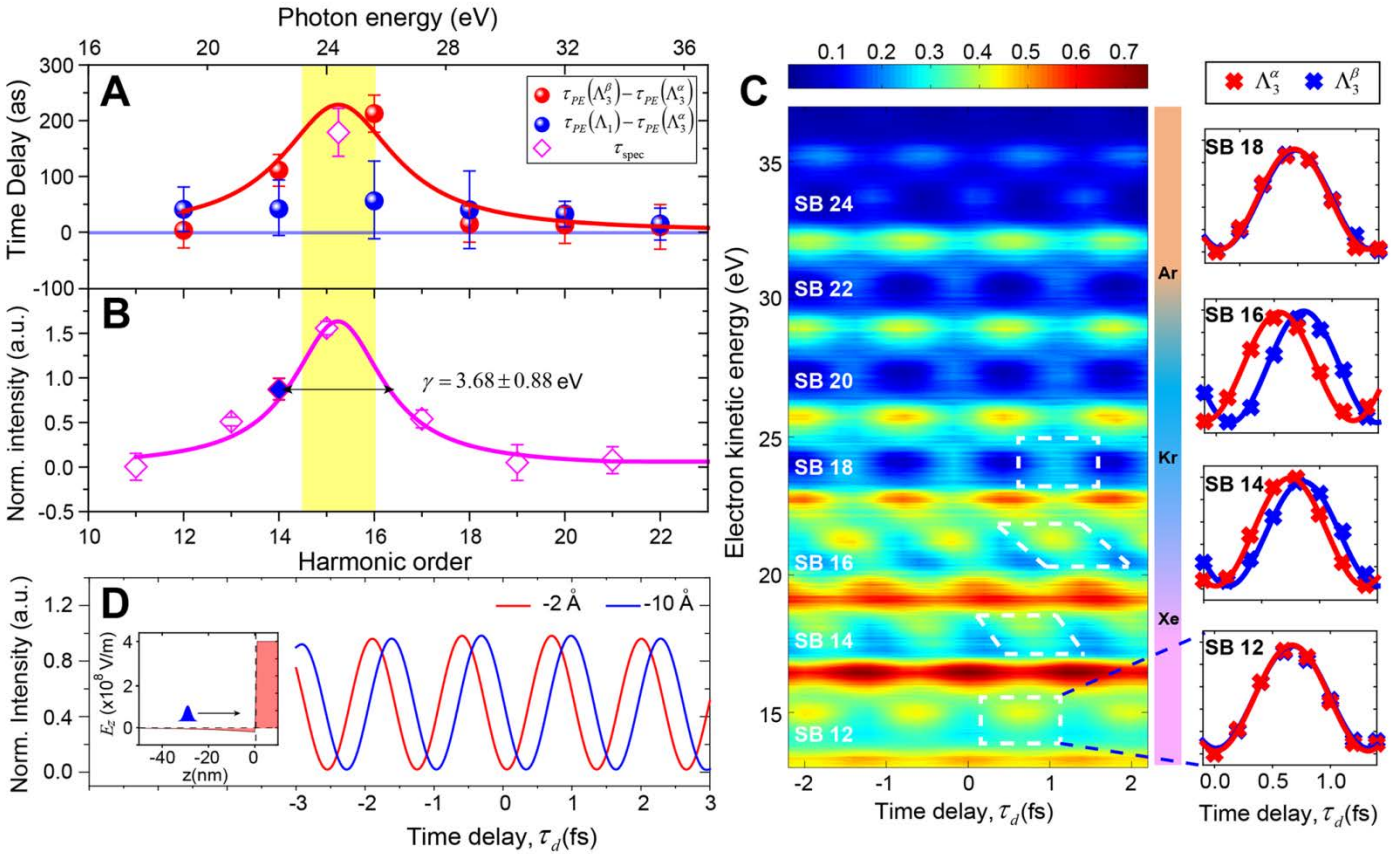

Fig. 3. Direct time-domain measurement of the final-state lifetime. (**A**) Photoemission time delays $\tau_{PE}\left(\Lambda_3^{\beta}\right)-\tau_{PE}\left(\Lambda_3^{\alpha}\right)$ and $\tau_{PE}\left(\Lambda_1\right)-\tau_{PE}\left(\Lambda_3^{\alpha}\right)$ as a function of photon energy, clearly showing an increase in lifetime by 212 ± 30 as when the final state corresponds to a short-lived excited state in the band structure. The error bars represent the standard deviations of time delays extracted from more than 200 individual scans. Red solid line - Lorentzian curve with the same linewidth as in (B). (**B**) Spectral intensity of the Λ_3^{β} initial band as a function of photon energy. The blue point (14th order) is obtained from 390 nm driven HHG. The error bars represent the fitting uncertainties of the photoelectron yield from individual photoelectron spectra that were used to extract each point (see supplementary materials). The pink line represents a Lorentzian fit, yielding a linewidth of γ = 3.68 eV. (**C**) 2D map of photoelectron yields as a function of photoelectron energy and pump-probe time delay τ_d, excited by s-polarized HHG. To enhance the color contrast, 90% of the ground-state spectrum is subtracted to visualize the interferogram. The relative delays between photoelectrons from the Λ_3^{α} and Λ_3^{β} initial bands are manifested as a large offset in oscillations in the side bands (white dashed). A zoom-in view in both energy and time delay at the resonant energy is plotted in fig. S5D. 1D lineouts for Λ_3^{α} and Λ_3^{β} initial bands in the corresponding regions are plotted in the right panel. (**D**) Results of 1D semiclassical simulations. Photoelectrons emitted 10 Å below the surface are delayed by 267 attoseconds compared to those emitted from 2 Å. Inset: profile of the dressing field strength normal to surface (E_z) across the interface.

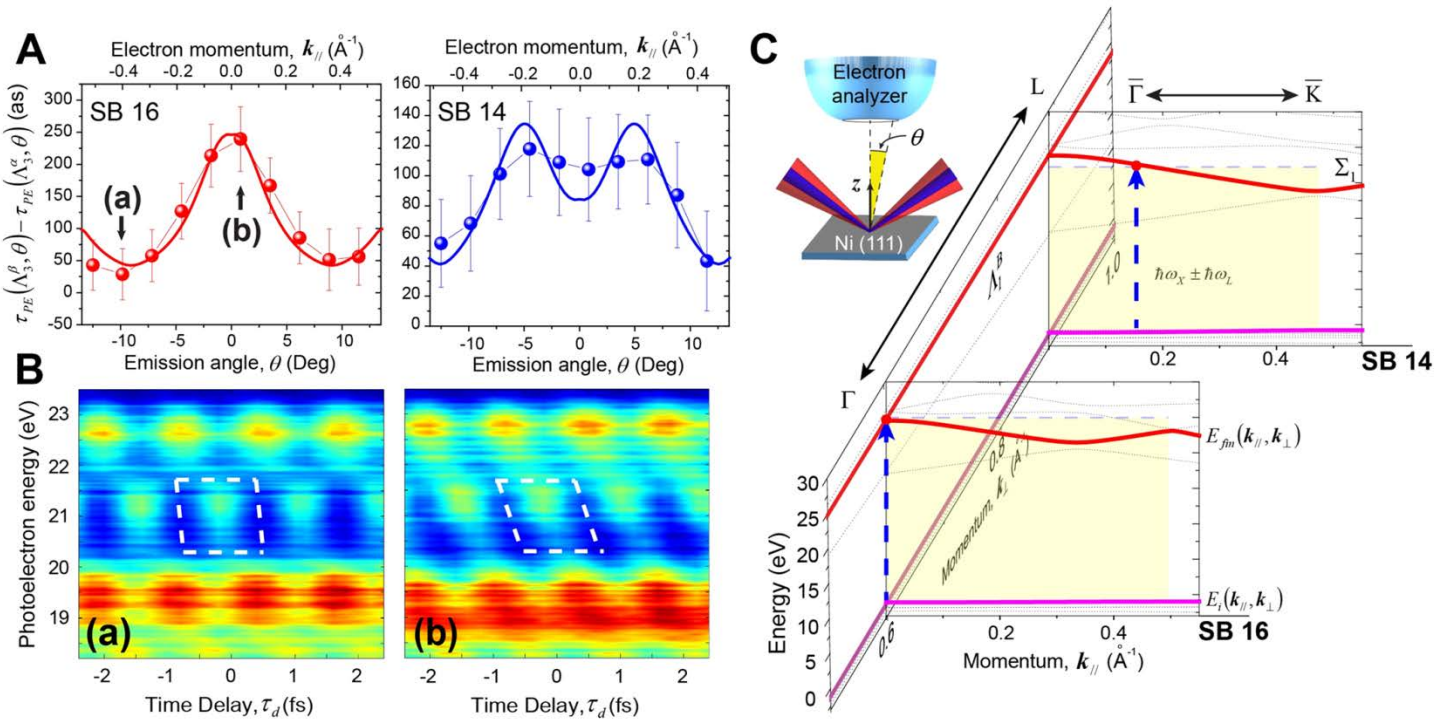

Fig. 4. Angle-dependent photoemission time delays. (**A**) Angle-dependent photoemission time delay $\tau_{PE}\left(\Lambda_3^\beta,\theta\right)-\tau_{PE}\left(\Lambda_3^\alpha,\theta\right)$ for SB 16 and 14 obtained using s-polarized HHG. The experimental data are points, while the solid lines are a fit to the final-state band structure obtained from our model and DFT calculations (see supplementary materials). The error bars represent the standard deviations of the time delays extracted from more than 200 individual scans. (**B**) Typical RABBITT interferograms for SB 16 with emission angles [(a) and (b)] labeled in (A). The offset in oscillations is highlighted with white dashed boxes. (**C**) Illustration of direct transitions in the direction $\bar{\Gamma}-\bar{K}$ for SB 14 and 16. Because different photon energies are used for these two side bands, different $k_\perp$ along the Γ-L direction are assigned according to the band-mapping results in Fig. 2B. The initial and final bands are highlighted by thick solid lines and the binding energy of the initial band (pink) is corrected according to the binding energy obtained in our experiments. The transitions are labeled as dashed arrows. Inset: Experimental geometry: IR and HHG beams are focused onto a Ni (111) surface at a 45° incident angle. θ is assigned to the emission angle of photoelectrons relative to the sample normal direction (**z**).